

# A 44-minute periodic radio transient in a supernova remnant

Di Li<sup>1,2,3†</sup>, Mao Yuan<sup>4,5†</sup>, Lin Wu<sup>4,5†</sup>, Jingye Yan<sup>4,5\*</sup>, Xuning Lv<sup>4,5\*</sup>, Chao-Wei Tsai<sup>2,6</sup>,  
 Pei Wang<sup>2,6</sup>, Weiwei Zhu<sup>2,6</sup>, Li Deng<sup>4,5</sup>, Ailan Lan<sup>4,5</sup>, Renxin Xu<sup>7,8,9</sup>, Xianglei Chen<sup>2</sup>,  
 Lingqi Meng<sup>2,10</sup>, Jian Li<sup>11</sup>, Xiangdong Li<sup>12,13</sup>, Ping Zhou<sup>12,13</sup>, Haoran Yang<sup>12,13</sup>,  
 Mengyao Xue<sup>2</sup>, Jiguang Lu<sup>2</sup>, Chenchen Miao<sup>3</sup>, Weiyang Wang<sup>10</sup>, Jiarui Niu<sup>2</sup>,  
 Ziyao Fang<sup>2,10</sup>, Qiuyang Fu<sup>2,10</sup>, Yi Feng<sup>3</sup>, Peijin Zhang<sup>14</sup>, Jinchen Jiang<sup>2</sup>, Xueli Miao<sup>2</sup>,  
 Yu Chen<sup>4,5</sup>, Lingchen Sun<sup>4,5</sup>, Yang Yang<sup>4,5</sup>, Xiang Deng<sup>4,5</sup>, Shi Dai<sup>15,16</sup>, Xue Chen<sup>17</sup>,  
 Jumei Yao<sup>18</sup>, Yujie Liu<sup>4,5</sup>, Changheng Li<sup>4,5</sup>, Minglu Zhang<sup>4,5</sup>, Yiwen Yang<sup>4,5</sup>,  
 Yucheng Zhou<sup>4,5</sup>, Yiyizhou<sup>4,5</sup>, Yongkun Zhang<sup>2</sup>, Chenhui Niu<sup>19</sup>, Rushuang Zhao<sup>20</sup>,  
 Lei Zhang<sup>2,21</sup>, Bo Peng<sup>2</sup>, Ji Wu<sup>4,5</sup>, Chi Wang<sup>4,5</sup>

<sup>1</sup>Department of Astronomy, Tsinghua University, Beijing 100084, China.

<sup>2</sup>National Astronomical Observatories, Chinese Academy of Sciences, Beijing 100101, China.

<sup>3</sup>Zhejiang Lab, Hangzhou, Zhejiang 311121, China.

<sup>4</sup>State Key Laboratory of Space Weather, Chinese Academy of Sciences, Beijing 100190, China.

<sup>5</sup>National Space Science Center, Chinese Academy of Sciences, Beijing 100190, China.

<sup>6</sup>Institute for Frontiers in Astronomy and Astrophysics, Beijing Normal University, Beijing 102206, China.

<sup>7</sup>Department of Astronomy, Peking University, Beijing 100871, China.

<sup>8</sup>Kavli Institute for Astronomy and Astrophysics, Peking University, Beijing 100871, China.

<sup>9</sup>State Key Laboratory of Nuclear Physics and Technology, School of Physics,

Peking University, Beijing 100871, China.

<sup>10</sup>University of Chinese Academy of Sciences, Beijing 100049, China.

<sup>11</sup>Department of Astronomy, School of Physical Sciences, University of Science and Technology of China,  
Hefei 230026, China.

<sup>12</sup>School of Astronomy and Space Science, Nanjing University, Nanjing 210023, China.

<sup>13</sup>Key Laboratory of Modern Astronomy and Astrophysics (Nanjing University),  
Ministry of Education, Nanjing 210023, China.

<sup>14</sup>New Jersey Institute of Technology, Newark NJ 07102, US.

<sup>15</sup>Western Sydney University, Locked Bag 1797, Penrith South DC, NSW 2751, Australia.

<sup>16</sup>School of Science, CSIRO Space and Astronomy, Australia Telescope National Facility,  
Epping, NSW 1710, Australia.

<sup>17</sup>Beijing Institute of Technology Chongqing Innovation Center, Chongqing, China.

<sup>18</sup>Xinjiang Astronomical Observatory, Chinese Academy of Sciences, Urumqi, Xinjiang 830011, China.

<sup>19</sup>Center China Normal University, Wuhan 430079, China.

<sup>20</sup>Guizhou Normal University, Guiyang 550001, China.

<sup>21</sup>Centre for Astrophysics and Supercomputing, Swinburne University of Technology,  
P.O. Box 218, Hawthorn, VIC 3122, Australia.

\*Corresponding author. Email: yanjingye@nssc.ac.cn

†These authors contributed equally to this work.

**Long-period radio transients (LPTs) are a newly discovered class of radio emitters with yet incomprehensibly long rotation periods, ranging from minutes to hours. The astrophysical nature of their isolated counterparts remains undetermined. We report a new LPT, DART J1832-0911 ( $2656.23 \pm 0.15$  s period), the first evidence associating such objects to supernova remnants (SNRs). Its dispersion measure distance aligns well with the distance of the SNR, confirming its**

**origin from a supernova explosion. The source displays either phase-locked circularly polarized emission or nearly 100% linear polarization in radio bands. No detectable optical counterpart was found, even with a 10m-class telescope. The J1832-0911’s SNR association, stable, highly polarized emission, and abnormally long period strongly favor its origin from a young neutron star, whose spin has been braked, possibly by interaction with supernova’s fallback materials. This discovery provides critical insights into the nature of ultra-long period transients and their evolutionary link to stellar remnants.**

Long-period radio transients (LPTs) are a new class of periodic radio emitters, characterized by ultra-long rotation periods and strong magnetic fields. These features place LPTs significantly outside the conventional framework of rotation-powered neutron star pulsars or white dwarfs (1–4). As for their isolated stellar candidates, the two primary models—spin-down powered pulsars and white dwarfs—each face significant challenges in explaining the observed emissions if they independently evolve in a traditional way: losing rotation energy through radio emission. Neutron stars with ultra-long periods typically fall below the so-called “death line”, where their rotational energy becomes insufficient to sustain coherent radio emission (5–7), while white dwarfs often have insufficient magnetic fields to produce the observed periodic, coherent emissions (4). Among reported LPT cases, four are identified as dwarf binary systems where accretion processes plays a role in driving the observed emissions (8–11), while four are isolated sources: GLEAM-X J162759.5-523504.3 (18.18 min) (1), GPM J1839-10 (21 min) (2), ASKAP J1935+2148 (53 min) (3), CHIME J0630+25 (7 min) (12). Although theoretical models lean toward isolated LPTs being magnetars (i.e. neutron stars with strong magnetic field), direct observational evidence and evolution studies remain limited.

## **DART Observation**

We report a new LPT in a supernova remnant, DART J1832-0911, detected by DAocheng Radio Telescope (DART) (see supplementary material) with interferometric imaging across a frequency range of 149-459 MHz. The first pulse was detected on Modified Julian Date (MJD) 60374. From MJD 60401 and MJD 60443, we conducted continuous observations of the transient using an interferometric imaging technique, with full polarization and at double center frequency. The

recorded pulses showed an estimated peak flux density between 0.5–2 Jy. After this period, the transient entered a long-period quiescent state, as recorded by DART observation.

The interferometric image allowed us to determine the celestial coordinates to be RA=18h32m48.8s ( $\pm 2''$ ) and DEC=-09d11m34s ( $\pm 8''$ ), situating it within the projected region of supernova remnant G22.7-0.2. Top panel in Fig.1 displays the pulse-on image of DART J1832-0911 at 425 MHz. The bottom panel shows the observed single pulses in two Stokes components. Additional pulse profile shapes are provided in the supplementary material (Fig.S1). All pulse series presented in this study have been aligned through periodic folding and corrected for delay time. By analyzing the time of arrival (TOA) of single pulses recorded by DART, we derive a spin period of  $P = 2656.23 \pm 0.15$  s with an estimated period derivative of  $\dot{P} < 5 \times 10^{-9}$  s/s. Fig.2 displays the  $P$ - $\dot{P}$  diagram of DART J1832-0911 as well as other LPTs.

## FAST Observation

To further investigate, we used the Five-hundred-meter Aperture Spherical Telescope (FAST) to observe the source at L-band during DART’s non-detection period on MJD 60559. During a 1-hour observation, we detected a short pulse with a peak flux density of approximately 94 mJy. The duration of the pulse (i.e. the pulse width) is 0.2 s, just 0.007% of the rotation period. This could point to a highly energetic and sharp emission event occurring at the strong magnetic field, like the dwarf pulse emission process of a neutron star (13, 14).

We folded the time series based on the ephemeris derived from DART observations and found that the TOA of this pulse is within the predicted emission phase. This short pulse is shown in Fig.3. The rotation measure (RM) of this pulse is  $105 \pm 0.07$  rad m<sup>-2</sup>. A summary of the measured parameters of this transient is provided in Table.1.

## Optical and X-ray Counterpart Search

We conducted an optical observation using the Gran Telescopio Canarias (GTC) on 30 July , 2024. The integration time for this observation was 1.25 hours. We conformed no counterparts in optical observation.

An  $r$ -band image of the DART source location was obtained using the broad-band imaging mode

of OSIRIS+ on the GTC. As shown in Fig.4, there are two optical candidates within the designated zone. However, the light curves of these candidates show no periodic variations on timescales of tens of minutes, indicating they are not associated with DART J1832-0911. Given an upper limit of 26.6 magnitudes for the GTC observations and assuming a white dwarf radius of  $r = 0.2R_{\odot}$  at a distance of 4.5 kpc, any WD detectable by the GTC would have an effective temperature below approximately  $T_{\text{eff}} \sim 17000\text{K}$ , indicating an evolution age at hundreds of millions years (see supplementary material). The absence of an optical counterpart supports the possibility of a compact neutron star rather than a WD. Additionally, our analysis shows that a spin-down powered WD would be unable to account for the observed emission power of a transient with characters like those of DART J1832-0911 (see supplementary material).

We searched for an X-ray counterpart using archival data from the XMM-Newton observatory, obtained on March 13, 2011 (Observation ID: 0654480101). The observation had an exposure time of  $1.54 \times 10^4$  s and covered the source with both XMM-PN and XMM-MOS2 detectors in the 0.2-10keV. Within the positional uncertainty of DART J1832-0911, only a single photon was detected by XMM-PN (see Fig.S8 in supplementary materia). Consequently, no X-ray counterpart was identified for either the transient or the associated SNR region. This yields an upper limit of  $6.648 \times 10^{-14}$  ergs  $\text{cm}^2 \text{ s}^{-1}$  in 0.2-10 keV at a 99% confidence level.

We suggest that the absence of X-ray detection may result from an unsuitable temporal observation window for the history data or inherently weak or absent X-ray emission from this source.

## Dispersion Measure and SNR Association Analysis

We calculated the dispersion measure (DM) using dual-frequency pulse series from DART and the short pulse spectra of FAST. By relating the TOA delay to the dispersion effect observed at two simultaneous frequencies, we obtained a DM of  $480 \pm 45 \text{ pc} \cdot \text{cm}^{-3}$ . A DM search of the FAST spectra yielded  $464.5 \pm 0.7 \text{ pc} \cdot \text{cm}^{-3}$ . These measurements from the two observatories are consistent with the 1 sigma error. Given the broader bandwidth and finer temporal resolution of FAST, we consider this result to be the precise DM for DART J1832-0911.

Based on this DM, we estimated the distance to DART J1832-0911, finding it consistent with the distance of SNR G22.7-0.2. Previous studies estimate the distance to SNR G22.7-0.2

at  $4.4 \pm 0.4$  kpc (15) or  $4.7 \pm 0.2$  kpc (16), based on molecular cloud analyses. Meanwhile, the DM-derived distance to DART J1832-0911, using the YMW16 electron-density model (17), is approximately 4.5 kpc, suggesting that this LPT resides within the SNR bubble. No other compact objects have been detected within this SNR.

We also investigated the X-ray emission of SNR G22.7-0.2 using data from XMM-Newton and previous studies. Our analysis, consistent with earlier research, reveals no evidence of extended X-ray emission within the radio range. The cessation of X-ray emission from the SNR suggests that the remnant’s shock velocity,  $V_s$ , has decreased below 200 km/s—insufficient to heat the gas to X-ray-emitting temperatures (18, 19). Consequently, we can reasonably infer that the SNR has entered the radioactive phase, during which the age of the SNR can be estimated  $t \sim 0.31R/V > 3 \times 10^4$  years where  $R = 18$  pc is the SNR radius. Assuming a lower limit for the shock velocity of 30 km/s (15), we obtain an upper age limit of  $t < 2 \times 10^5$  years.

## Radio Emission Properties

DART J1832-0911 displays a range of emission characteristics during its active radio period. Prior to either undetectable weak emission or nulling, the source undergoes mode changes modulated by variations in pulse width and strength, as illustrated in the bottom panel of Fig. 1. These time-dependent mode changes reveal an evolution from bright, wide pulses to weaker, narrower ones. In the wide mode, pulse widths range from 100 s to 300 s, with a flux density of about 2 Jy. In the narrow mode, pulse width narrows to approximately 40 s, and flux density increases to roughly 1 Jy. During the emission-quiescent state, as observed by DART, we captured a short-lived pulse by FAST. Within the expected periodic phase, this pulse lasted 0.2 s and exhibited a peak flux of  $\sim 94 \pm 27$  mJy. Such brief, isolated emission components have also been observed in other long-period transients (2, 3).

The polarization recorded of DART J1832-0911 presents unique properties as it significantly diverges from the other LPTs. While all reported isolated LPTs—except CHIME J0630+25 for which the research provided no polarization information—exhibit notable polarized components throughout their emission cycles, DART’s pulses show a sporadic distribution of polarization components. Additionally, many pulses are extremely poorly polarized throughout the entire phase.

Aside from a few sharp impulsive linear polarization (LP) components, we found no other LP emissions with a signal-to-noise ratio (S/N) greater than  $3\sigma$  for most pulses. Fig.S4 highlights two instances of narrow LP components with S/N of  $14.2\sigma$  (MJD 60416) and  $6.6\sigma$  (MJD 60421), respectively. Regarding circular polarization (CP), we observed that pulses in the wide mode exhibit narrow and phase-locked CP components, as illustrated in the bottom panel of Fig.1. The peak flux ratio of the highest CP components to the aligned total intensity reaches  $V/I \sim 64\%$ . Additionally, most CP components display sign reversal (see Fig.S4). The narrow width of the CP components, spanning less than 3% of the period, emphasizes a fixed circularly polarized emission zone in a limited region. Notably, the short-lived pulse detected by FAST is nearly 100% linearly polarized, and the PA is flat across the whole emission duration. Fig.3 shows the dynamic spectra and polarization properties of this pulse.

## **Stellar Origin and Evolution of DART J1832-0911**

The discovery of DART J1832-0911 strongly favors a young neutron star as one origin of long period radio transients. The spatial association between this source and the SNR indicates that it is likely the stellar remains of a supernova explosion, specifically a neutron star rather than a white dwarf. Given the characteristic age of both DART J1832-0911 and SNR G22.7-0.2, it is reasonable to conclude that DART J1832-0911 is a young neutron star. The emission properties further suggest a pulsar-like emitter of DART J1832-0911. The narrow, phase-locked CP indicates a stable geometric structure of the magnetic field of DART J1832-0911 even at small scales. This stability argues against models that rely on dynamic magnetic fields as the primary driver of radio emission, such as star flares (20) and dwarf binary systems (8, 10). The nearly 100% linearly polarized burst signals support both theoretical radio emission mechanism and observation related to magnetars (21–24), which is believed to be a kind of young neutron stars (25). Such short-lived pulse emitted during a emission-dull or -quiescent state is similar to the dwarf pulse observed during pulsars' nulling period (13, 14, 26–28). These emissions are believed to arise from rain-like drops of particles formed via pair production near the neutron star surface (13, 14).

A neutron star nature of LPTs significantly challenges conventional evolution models of fast spinning neutron star scenarios (4), which typically have rotation periods of less than a few minutes,

**Table 1: Measured parameters of DART J1832-0911 from the DART and FAST observation.**

Parameter	DART	FAST
	149-459 MHz	1-1.5 GHz
Period derivative (s/s)	$5 \times 10^{-9}$	-
DM (pc cm <sup>-3</sup> )	480±45	464.5±0.7
RM (rad m <sup>-2</sup> )	-	+105 ± 0.07
Pulse Width (s)	40-250	0.2
Peak flux density (Jy)	0.5-2	0.096±0.027

as illustrated in Fig.2. Theoretically, neutron stars—formed as remnants of supernova explosions—are born with fast spin periods on the order of milliseconds if they inherit most or all of the angular momentum from their progenitors. Consequently, the emergence of LPTs suggests that these stars could form under two possible conditions: either with a significant loss of angular momentum from their progenitors such as neutrino emission (29, 30), or through some rotational braking process during their spin evolution (see (31) for a review).

Based on the fact that DART J1832-0911 is surrounded by supernova remnant matters, the braking process of a neutron star spun down by its surrounding supernova fallback disc (32–34) should be the most reasonable explanation for the long period. We simulate the reasonable period range based on a fallback disc model (34), as shown in Fig.2. The results suggest that the observed LPTs could be well explained in the period between  $10^4$  and  $10^5$  years after the supernova explosion. Therefore, the association between DART J1832-0911 and SNR G22.7-0.2, with an age estimate ranging from  $3 \times 10^4$  to  $2 \times 10^5$  years, could further support the hypothesis that such LPTs may originate from interactions between young neutron stars and fallback discs.

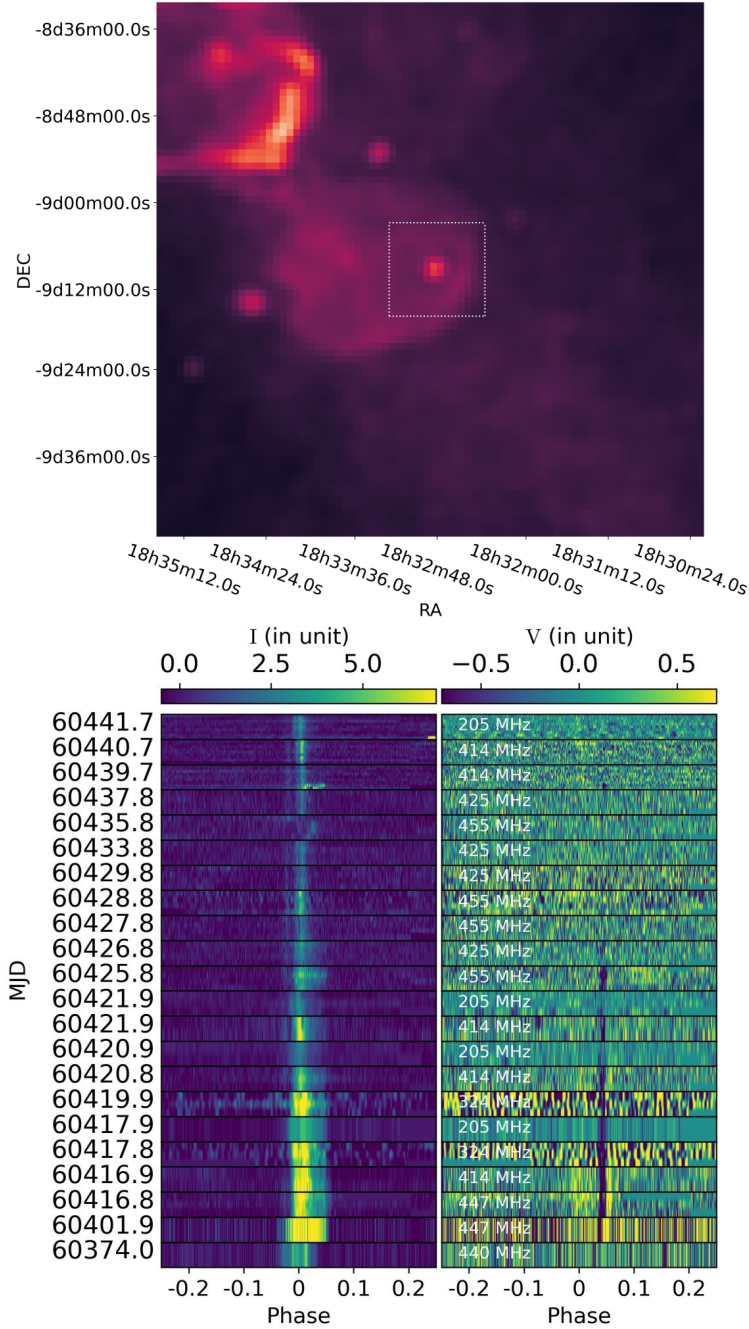


**Figure 1: DART observation of J1832-0911.** The top panel is the radio image of DART J1832-0911. The source is indicated in the white dotted box, within the SNR  $G_{22.7-0.2}$ . The bottom panel exhibits a single pulse stack in total intensity (left panel: “Stokes I”) and phase-locked circular polarization (right panel: “Stokes V”), sorted by observed MJD. Each sub-panel corresponds to single pulses detected on each observation day, labeled with the barycentric MJD (left) and observed frequency range (right).

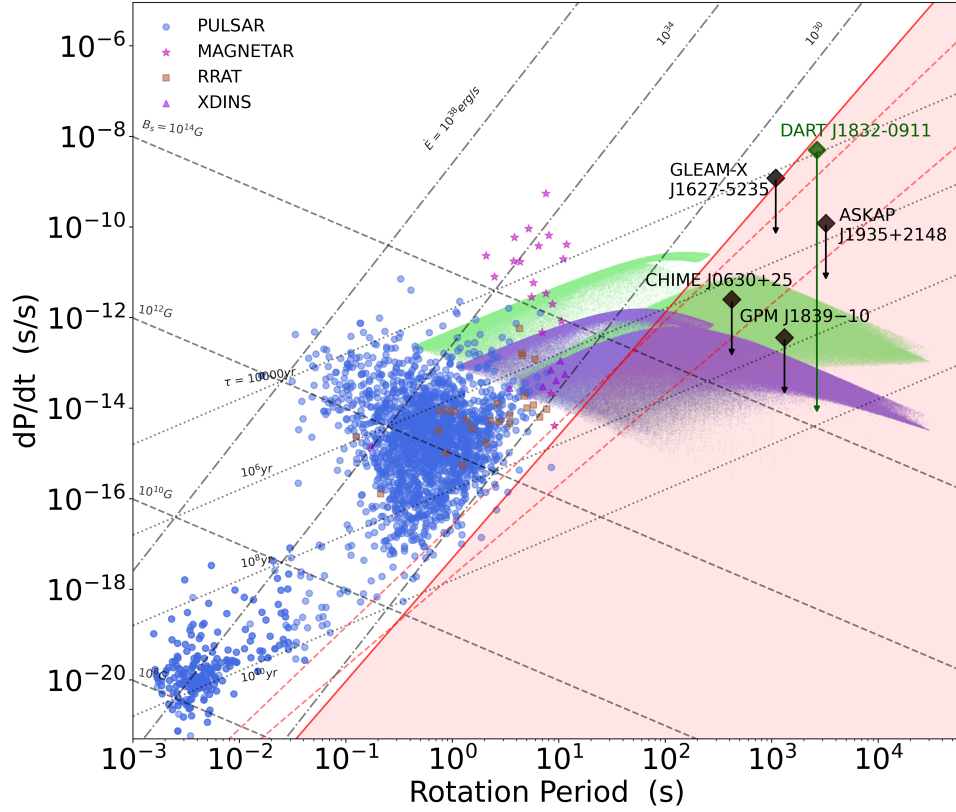


**Figure 2: P-Pdot diagram of radio transients under a spin-down powered scenario.** DART J1832-0911 and other reported isolated long-period radio transients are marked by diamonds with arrows indicating their upper limits on period derivatives. The other types of transients are pulsars (blue dots), magnetars (purple stars), RRATs (brown squares), and XDINS (light purple triangles). The solid red line represents the theoretical death line for spin-down powered neutron stars with a pure dipole magnetic field (5), while the dashed red lines show the death lines for neutron stars with multipole fields (35). The green and purple shaded areas indicate the period ranges influenced by supernova fallback disk accretion from simulations (see supplementary material). These regions correspond to supernova remnant ages of  $3 \times 10^4$  and  $2 \times 10^5$  years.

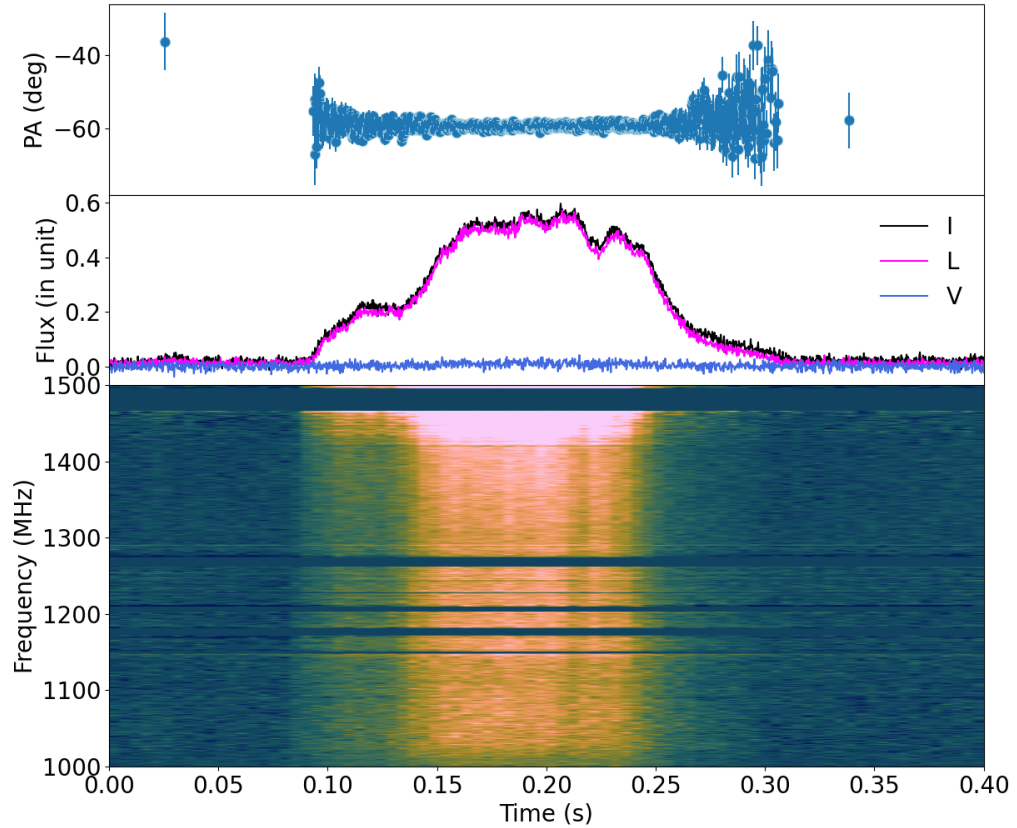


**Figure 3: The short pulse detected by FAST.** The top panel displays the linear polarization angle, while the middle panel presents the pulse profiles, including the total intensity(I), linear polarization(L), and circular polarization(V).

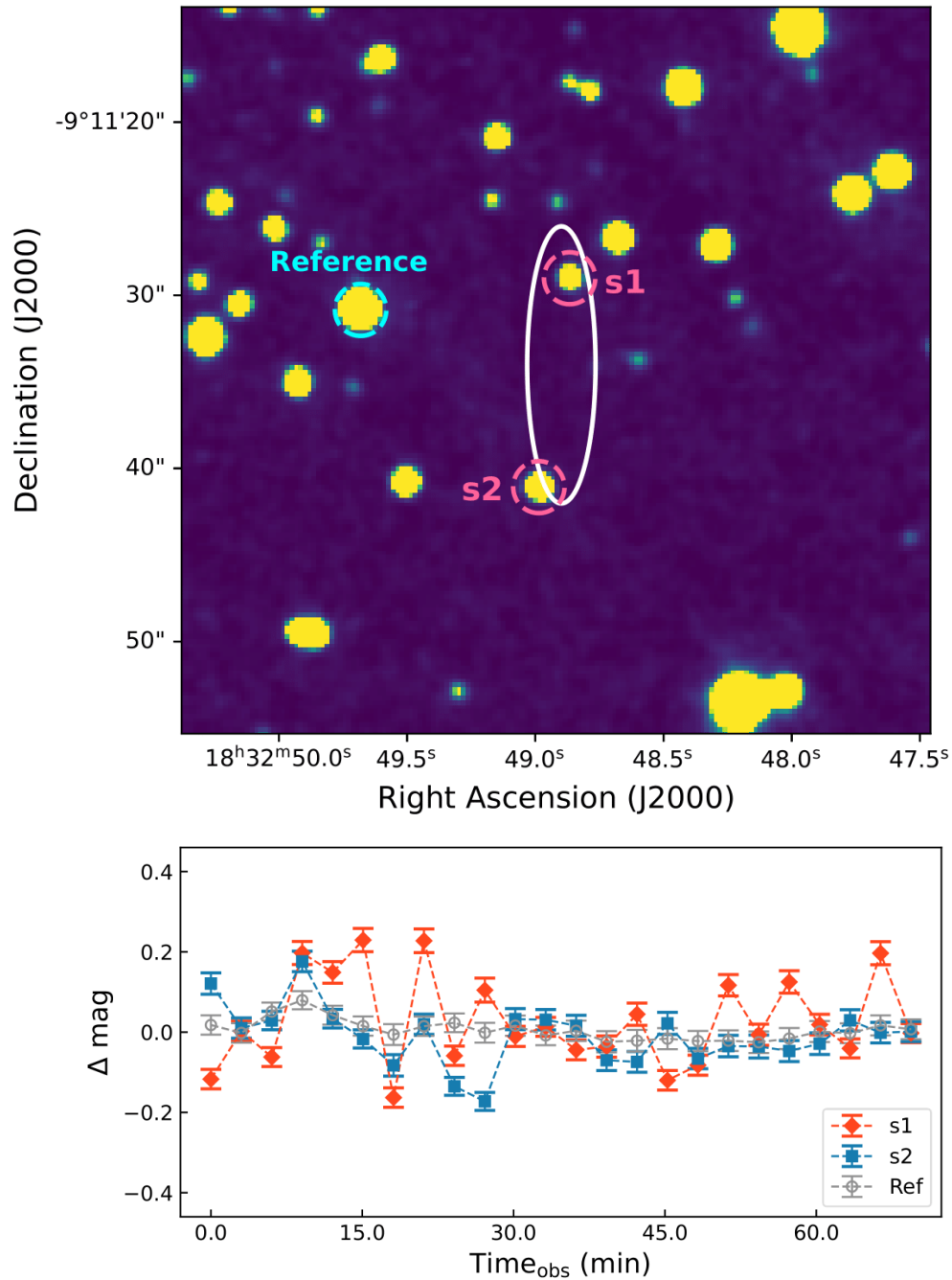


**Figure 4: Optical search of the DART source.** The top panel shows the GTC  $r$ -band image of the source’s celestial field. The white ellipse indicates the positional uncertainty of DART J1832-0911, with  $\Delta\text{RA} = 2''$  and  $\Delta\text{DEC} = 8''$ . The bottom panel presents the optical light curves of the reference star and a nearby candidate marked in the top panel. Neither light curve exhibits periodicity or variation timescale comparable to that of DART J1832-0911.

## References and Notes

1. N. Hurley-Walker, *et al.*, A radio transient with unusually slow periodic emission. *Nature* **601** (7894), 526–530 (2022).
2. N. Hurley-Walker, *et al.*, A long-period radio transient active for three decades. *Nature* **619** (7970), 487–490 (2023).
3. M. Caleb, *et al.*, An emission-state-switching radio transient with a 54-minute period. *Nature Astronomy* pp. 1–10 (2024).
4. N. Rea, *et al.*, Long-period radio pulsars: population study in the neutron star and white dwarf rotating dipole scenarios. *The Astrophysical Journal* **961** (2), 214 (2024).
5. K. Chen, M. Ruderman, Pulsar death lines and death valley. *Astrophysical Journal, Part 1 (ISSN 0004-637X)*, vol. 402, no. 1, p. 264-270. **402**, 264–270 (1993).
6. M. Young, R. N. Manchester, S. Johnston, A radio pulsar with an 8.5-second period that challenges emission models. *Nature* **400** (6747), 848–849 (1999).
7. M. Caleb, *et al.*, Discovery of a radio-emitting neutron star with an ultra-long spin period of 76 s. *Nature Astronomy* **6** (7), 828–836 (2022).
8. T. Marsh, *et al.*, A radio-pulsing white dwarf binary star. *Nature* **537** (7620), 374–377 (2016).
9. I. Pelisoli, *et al.*, A 5.3-min-period pulsing white dwarf in a binary detected from radio to X-rays. *Nature Astronomy* **7** (8), 931–942 (2023).
10. I. de Ruiter, *et al.*, A white dwarf binary showing sporadic radio pulses at the orbital period. *arXiv preprint arXiv:2408.11536* (2024).
11. N. Hurley-Walker, *et al.*, A 2.9-hour periodic radio transient with an optical counterpart. *arXiv preprint arXiv:2408.15757* (2024).
12. F. A. Dong, *et al.*, The discovery of a nearby 421~ s transient with CHIME/FRB/Pulsar. *arXiv preprint arXiv:2407.07480* (2024).

13. X. Chen, *et al.*, Strong and weak pulsar radio emission due to thunderstorms and raindrops of particles in the magnetosphere. *Nature Astronomy* **7** (10), 1235–1244 (2023).
14. Y. Yan, *et al.*, Dwarf Pulses of 10 Pulsars Detected by FAST. *The Astrophysical Journal* **965** (1), 25 (2024).
15. Y. Su, J. Yang, X. Zhou, P. Zhou, Y. Chen, INTERACTION BETWEEN SUPERNOVA REMNANT G22. 7- 0.2 AND THE AMBIENT MOLECULAR CLOUDS. *The Astrophysical Journal* **796** (2), 122 (2014).
16. S. Ranasinghe, D. Leahy, Revised distances to 21 supernova remnants. *The Astronomical Journal* **155** (5), 204 (2018).
17. J. Yao, R. Manchester, N. Wang, A new electron-density model for estimation of pulsar and FRB distances. *The Astrophysical Journal* **835** (1), 29 (2017).
18. C. F. McKee, X-ray emission from an inward-propagating shock in young supernova remnants. *Astrophysical Journal, Vol. 188, pp. 335-340 (1974)* **188**, 335–340 (1974).
19. R. A. Chevalier, Supernova remnants in molecular clouds. *The Astrophysical Journal* **511** (2), 798 (1999).
20. A. O. Benz, M. Güdel, Physical processes in magnetically driven flares on the sun, stars, and young stellar objects. *Annual Review of Astronomy and Astrophysics* **48** (1), 241–287 (2010).
21. F. Camilo, *et al.*, Transient pulsed radio emission from a magnetar. *Nature* **442** (7105), 892–895 (2006).
22. F. Camilo, *et al.*, Polarized Radio Emission from the Magnetar XTE J1810–197. *The Astrophysical Journal* **659** (1), L37 (2007).
23. M. Kramer, B. Stappers, A. Jessner, A. Lyne, C. Jordan, Polarized radio emission from a magnetar. *Monthly Notices of the Royal Astronomical Society* **377** (1), 107–119 (2007).
24. L. Levin, *et al.*, Radio emission evolution, polarimetry and multifrequency single pulse analysis of the radio magnetar PSR J1622- 4950. *Monthly Notices of the Royal Astronomical Society* **422** (3), 2489–2500 (2012).

25. V. M. Kaspi, A. M. Beloborodov, Magnetars. *Annual Review of Astronomy and Astrophysics* **55** (1), 261–301 (2017).
26. Z. Srostlik, J. M. Rankin, Core and conal component analysis of pulsar B1237+ 25. *Monthly Notices of the Royal Astronomical Society* **362** (4), 1121–1133 (2005).
27. I. M. Kloumann, J. M. Rankin, On the long and short nulls, modes and interpulse emission of radio pulsar B1944+ 17. *Monthly Notices of the Royal Astronomical Society* **408** (1), 40–52 (2010).
28. A. Esamdin, D. Abdurixit, R. Manchester, H. Niu, PSR B0826-34: sometimes a rotating radio transient. *The Astrophysical Journal Letters* **759** (1), L3 (2012).
29. R. Epstein, Neutrino angular momentum loss in rotating stars. *Astrophysical Journal, Part 2-Letters to the Editor, vol. 219, Jan. 1, 1978, p. L39-L41.* **219**, L39–L41 (1978).
30. G. Camelió, L. Gualtieri, J. A. Pons, V. Ferrari, Spin evolution of a proto-neutron star. *Physical Review D* **94** (2), 024008 (2016).
31. A. Heger, S. Woosley, H. Spruit, Presupernova evolution of differentially rotating massive stars including magnetic fields. *The Astrophysical Journal* **626** (1), 350 (2005).
32. K. Menou, R. Perna, L. Hernquist, Stability and evolution of supernova fallback disks. *The Astrophysical Journal* **559** (2), 1032 (2001).
33. M. Ronchi, N. Rea, V. Graber, N. Hurley-Walker, Long-period pulsars as possible outcomes of supernova fallback accretion. *The Astrophysical Journal* **934** (2), 184 (2022).
34. H.-R. Yang, X.-D. Li, S.-J. Gao, K. Xu, Instability in Supernova Fallback Disks and Its Effect on the Formation of Ultralong Period Pulsars. *The Astrophysical Journal* **976** (1), 77 (2024).
35. B. Zhang, A. K. Harding, A. G. Muslimov, Radio pulsar death line revisited: is PSR J2144–3933 anomalous? *The Astrophysical Journal* **531** (2), L135 (2000).
36. J. Yan, *et al.*, A super radio camera with a one-kilometre lens. *Nature Astronomy* **7** (6), 750–750 (2023).

37. C. Wang, *et al.*, China's ground-based space environment monitoring network—Chinese Meridian Project (CMP). *Space Weather* **22** (7), e2024SW003972 (2024).
38. P. Jiang, *et al.*, The fundamental performance of FAST with 19-beam receiver at L band. *Research in Astronomy and Astrophysics* **20** (5), 064 (2020).
39. M. Craig, *et al.*, astropy/ccdproc: v1. 3.0. post1. *Zenodo* (2017).
40. S. Hoffmann, *et al.*, New Drizzlepac Handbook Version 2.0 Released In Hdox: Updated Documentation For HST Image Analysis, in *American Astronomical Society Meeting Abstracts*, vol. 53 (2021), pp. 216–02.
41. L. Bradley, *et al.*, Photutils: Photometry tools. *Astrophysics Source Code Library* pp. ascl–1609 (2016).
42. A. W. Hotan, W. van Straten, R. N. Manchester, PSRCHIVE and PSRFITS: an open approach to radio pulsar data storage and analysis. *Publications of the Astronomical Society of Australia* **21** (3), 302–309 (2004).
43. W. van Straten, P. Demorest, S. Osłowski, Pulsar data analysis with PSRCHIVE. *arXiv preprint arXiv:1205.6276* (2012).
44. D. Michilli, *et al.*, An extreme magneto-ionic environment associated with the fast radio burst source FRB 121102. *Nature* **553** (7687), 182–185 (2018).
45. B. Andersen, *et al.*, CHIME/FRB discovery of eight new repeating fast radio burst sources. *The Astrophysical Journal Letters* **885** (1), L24 (2019).
46. G. Hilmarsson, L. Spitler, R. Main, D. Li, Polarization properties of FRB 20201124A from detections with the Effelsberg 100-m radio telescope. *Monthly Notices of the Royal Astronomical Society* **508** (4), 5354–5361 (2021).
47. A. Jessner, *et al.*, Giant pulses with nanosecond time resolution detected from the Crab pulsar at 8.5 and 15.1 GHz. *Astronomy & Astrophysics* **524**, A60 (2010).
48. T. Hankins, J. Eilek, G. Jones, The Crab pulsar at centimeter wavelengths. II. Single pulses. *The Astrophysical Journal* **833** (1), 47 (2016).

49. W. Lu, P. Kumar, R. Narayan, Fast radio burst source properties from polarization measurements. *Monthly Notices of the Royal Astronomical Society* **483** (1), 359–369 (2019).
50. J. Ostriker, J. Gunn, On the nature of pulsars. I. Theory. *Astrophysical Journal*, vol. 157, p. 1395 **157**, 1395 (1969).
51. I. Contopoulos, A. Spitkovsky, Revised pulsar spin-down. *The Astrophysical Journal* **643** (2), 1139 (2006).
52. I. Contopoulos, C. Kalapotharakos, D. Kazanas, A new standard pulsar magnetosphere. *The Astrophysical Journal* **781** (1), 46 (2014).
53. A. Szary, B. Zhang, G. I. Melikidze, J. Gil, R.-X. Xu, Radio efficiency of pulsars. *The Astrophysical Journal* **784** (1), 59 (2014).
54. A. Biryukov, P. Abolmasov, Magnetic angle evolution in accreting neutron stars. *Monthly Notices of the Royal Astronomical Society* **505** (2), 1775–1786 (2021).
55. Ü. Ertan, K. Y. Ekşi, M. H. Erkut, M. A. Alpar, On the evolution of anomalous x-ray pulsars and soft gamma-ray repeaters with fall back disks. *The Astrophysical Journal* **702** (2), 1309 (2009).
56. L. Mestel, On the theory of white dwarf stars: I. the energy sources of white dwarfs. *Monthly Notices of the Royal Astronomical Society* **112** (6), 583–597 (1952).
57. L. G. Althaus, A. H. Córscico, J. Isern, E. García-Berro, Evolutionary and pulsational properties of white dwarf stars. *The Astronomy and Astrophysics Review* **18**, 471–566 (2010).
58. S. O. Kepler, *et al.*, White dwarf mass distribution in the SDSS. *Monthly Notices of the Royal Astronomical Society* **375** (4), 1315–1324 (2007).
59. J. L. Provencal, H. Shipman, E. Høg, P. Thejll, Testing the white dwarf mass-radius relation with Hipparcos. *The Astrophysical Journal* **494** (2), 759 (1998).

## **Supplementary materials**

Materials and Methods

Figs. S1 to S8

Tables S1

References (7-59)

## Supplementary Materials for

### A 44-minute periodic radio transient in a supernova remnant

Di Li<sup>1,2,3†</sup>, Mao Yuan<sup>4,5†</sup>, Lin Wu<sup>4,5†</sup>, Jingye Yan<sup>4,5\*</sup>, Xuning Lv<sup>4,5\*</sup>, Chao-Wei Tsai<sup>2,6</sup>, Pei Wang<sup>2,6</sup>, Weiwei Zhu<sup>2,6</sup>, Li Deng<sup>4,5</sup>, Ailan Lan<sup>4,5</sup>, Renxin Xu<sup>7,8,9</sup>, Xianglei Chen<sup>2</sup>, Lingqi Meng<sup>2,10</sup>, Jian Li<sup>11</sup>, Xiangdong Li<sup>12,13</sup>, Ping Zhou<sup>12,13</sup>, Haoran Yang<sup>12,13</sup>, Mengyao Xue<sup>2</sup>, Jiguang Lu<sup>2</sup>, Chenchen Miao<sup>3</sup>, Weiyang Wang<sup>10</sup>, Jiarui Niu<sup>2</sup>, Ziyao Fang<sup>2,10</sup>, Qiuyang Fu<sup>2,10</sup>, Yi Feng<sup>3</sup>, Peijin Zhang<sup>16</sup>, Jinchen Jiang<sup>2</sup>, Xueli Miao<sup>2</sup>, Yu Chen<sup>4,5</sup>, Lingchen Sun<sup>4,5</sup>, Yang Yang<sup>4,5</sup>, Xiang Deng<sup>4,5</sup>, Shi Dai<sup>14,15</sup>, Xue Chen<sup>17</sup>, Jumei Yao<sup>18</sup>, Yujie Liu<sup>4,5</sup>, Changheng Li<sup>4,5</sup>, Minglu Zhang<sup>4,5</sup>, Yiwen Yang<sup>4,5</sup>, Yucheng Zhou<sup>4,5</sup>, Yiyizhou<sup>4,5</sup>, Yongkun Zhang<sup>2</sup>, Chenhui Niu<sup>19</sup>, Rushuang Zhao<sup>20</sup>, Lei Zhang<sup>2,21</sup>, Bo Peng<sup>2</sup>, Ji Wu<sup>4,5</sup>, Chi Wang<sup>4,5</sup>

#### **This PDF file includes:**

Materials and Methods

Figures S1 to S8

Tables S1

# Materials and Methods

## DART Observation & Data Reduction

DART (previously known as DSRT, for a detail description, see Yan et.al 2023 (36)) is a synthetic aperture circular array telescope completed in 2023 for dynamic solar imaging. Located in Daocheng, Sichuan Province, China, DART is part of the Chinese Meridian Project's key observation sites (37). The array consists of 313 parabolic antennas, each with a 6-meter aperture evenly distributed on a circle, forming a configuration with a diameter of 1 kilometer. We utilize DART to image the sky in the frequency band of 149-459 MHz. The maximum field of view (FOV) of DART at 150 MHz is approximately  $20^\circ \times 20^\circ$ . For the high-frequency band, the angular resolution is approximately 100 arc-seconds. By fitting the point spread function (PSF) of a bright point source within a 3 dB angular width, DART achieves a positional precision of a few arcseconds for point sources. The telescope's ability to produce continuous interferometric images with a temporal resolution as fast as 5 milliseconds makes it an exceptionally powerful tool for surveying dynamic phenomena across the Universe.

The DART backend simultaneously records interferometric visibilities at two distinct frequency channels, each with a bandwidth of 4 MHz. Consequently, multiple epochs at different central frequencies retrieve the frequency-dependent effect of dispersion.

For the majority of the data, we configure the integration time within a range from 100 to 500 milliseconds. For each observation, two center frequencies are selected from within the entire frequency band. Ultimately, a pulse series spanning from 190 MHz to 455 MHz is recorded. All these pulses are acquired with complete Stokes components. Fig.S1 showcases a portion of the pulse profile components.

In DART system, the polarimetric measurement accuracy of DART is achieved by amplitude and phase unbalance calibration with the external and internal calibration. Specifically, the measurement is composed by direct dual-pol observation(HH,VV) and full-polarimetric cross-correlation (HH,VV and HV). A post-data processing can finally covert the polarimetric measurement to the

Stokes parameters as the form like

$$\begin{aligned}
 I &= \frac{S_{HH} + S_{VV}}{2}, \\
 Q &= \frac{S_{HH} - S_{VV}}{2}, \\
 U &= \text{Re}(S_{HV}), \\
 V &= -\text{Im}(S_{HV}).
 \end{aligned} \tag{S1}$$

We illustrate the data processing chain in Fig.S3. The polarimetric measurement accuracy only depends on the amplitude and phase unbalance of the DART array. Polarimetric calibration of DART is applied by the channel-based systematic calibration. With the external and internal systematic calibration, the amplitude and phase accuracy of 0.2 dB and  $2.5^\circ$  between any pair of receivers is guaranteed. With the low residual calibration errors, the polarimetric measurement error of DART is lower than 5% (36).

## FAST Observation and Flux Estimation

We conducted a union observation of DART and FAST at MJD 60559, with the integration time at 1 hour. The FAST frequency band and sampling time are 1-1.5 GHz and 196 us. The 19-beam receiver of FAST adopts orthogonal linear polarisation feeds, the diode noise signal will be injected as the polarization calibrated reference before the target signal recording. We conduct the polarimetric calibration by using the PSRCHIVE software.

We estimated the flux density of the pulse based on its SNR, using the radiometer equation:

$$f_v = \frac{T_{\text{sys}} \cdot \text{SNR}}{G \sqrt{2B\Delta t}}, \tag{S2}$$

where  $T_{\text{sys}} \approx 24$  K and  $G \approx 16$  K/Jy represent the system temperature and gain of FAST (38), respectively.  $B, t$  are the bandwidth and temporal resolution of the observation.

## Parkes UWL Observation

We conducted a union observation of DART and Parkes at MJD 60425. We used Parkes to observe toward the initial position (RA = 18:32:45.0, Dec = -09:12:00.0) for 180 minutes starting from

MJD 60425.74625, during which the transient is on the radio-active epoch. We used the standard Parkes backend, Medusa, which applies automatic gain correction for each sub-integration (in a timescale of 0.524288 s). We restored the original result using the scale and offset value recorded in PSRFITS. We extract Parkes UWL subband 0 to 2 (frequency 704 – 1088 MHz) and frequency scrunch the entire 384 MHz. We used a time resolution of 0.524288 s, and applied Savitzky-Golay smooth with second-order polynomial fit and a window length of 51 time-samples.

We confirmed that no pulses with an SNR greater than 3 were detected, whereas DART was able to detect them. We contend that the failure to detect these pulses is due to the automatic baseline correction employed by the backend of Parkes.

## GTC Observation

We obtained the  $r$ -band image of the DART source using the broad-band imaging mode of the OSIRIS+ on the Gran Telescopio CANARIAS (GTC) on 30 July 2024. The image was co-added using 24 single exposures of 150 s each to avoid sky saturation. A four-point dithering was used to avoid cosmic ray contamination. The total on-source time was 3600 s, and the observation duration lasted about 1.25 hr, including overheads. The observations were conducted under good weather conditions (seeing  $\sim 0.7''$ ). The data were first bias-subtracted, flat-fielded, cleaned of cosmic rays, and combined using the *ccdproc* (39) and *DrizzlePac* (40) packages following standard techniques. The sky background of the entire image was then modeled and subtracted, primarily using the *photutils* (41) package, following the instructions for modeling the complex 2D background in the Cross-Instrument section of the JWST Data Analysis Tool Notebooks<sup>1</sup>. The  $3\sigma$  detection limit of the co-added image is 24.8 mag, while the  $1\sigma$  upper limit of the background is 26.6 mag.

We searched for sources within a  $30''$  radius around the DART coordinates by performing aperture photometry on the co-added image using a  $2''$  radius. Additionally, we analyzed all 24 single exposures to check for light variability in the detected sources. No sources were found within  $2''$  of the DART coordinates. Fig. 4 shows the two nearest sources to the DART coordinates, along with the reference star. The light curves of these three sources are presented in Fig. 4. The

---

<sup>1</sup>[https://spacetelescope.github.io/jdat\\_notebooks/notebooks/cross\\_instrument/background\\_estimation\\_imaging/Imaging\\_Sky\\_Background\\_Estimation.html](https://spacetelescope.github.io/jdat_notebooks/notebooks/cross_instrument/background_estimation_imaging/Imaging_Sky_Background_Estimation.html)

$\Delta\text{mag}$  represents the discrepancies between the photometry of each single exposure and the mean magnitude during the observations. Extended Data Table S1 provides details on the two nearest targets.

The optical non-detection at the DART coordinates sets an upper limit on its optical counterparts. The radio emissions might originate from a faint dwarf star below our detection threshold, or from other objects not expected to be visible in optical observations, such as a neutron star. In the case of a faint white dwarf, assuming an upper limit of 26.6 mag and a white dwarf radius of  $r = 0.2R_{\odot}$ , the corresponding effective temperature would be  $T_{\text{eff}} \sim 17000\text{K}$  or lower.

## Timing Analysis

We derive the period through standard pulsar timing methods. Before the timing progress, we had transferred the local time (in MJD) to the barycenter frame of the solar system. We first use a prior period of 2656.2 s to adopt the single pulses from a continuous time series. Then, we select several pulses with high SNR and take their mean profile as the standard template, to cross-correlate any other pulses to determine the TOA for each pulse. Specifically, we calculated a series of correlations between any single pulse and the standard profile by shifting the bins (i.e. the TOAs) of single pulses. Then we fitted the relation of correlations versus TOAs by a Gaussian function and determined the proper TOA based on fitting result. The TOA errors are derived at a  $3\sigma$  level of Gaussian fitting.

We collect a group of TOAs covering about 3 months, a long nulling state prevents us for recording more data. We use the least-square timing method to fit TOAs and derive a period  $P$  at  $2656.23 \pm 0.15$  s. The period derivative we estimate is  $\dot{P} < 5 \times 10^{-9}$  s/s. It is important to mention that the fitted TOAs belong to pulses at a central frequency of 425 MHz, because we collected the largest number of pulses at this frequency. Fig.2 shows the P-Pdot diagram of DART J1832-0911. We also present another three reported LPRTs in the figure.

## Dispersion Measure (DM) and Rotation measure (RM)

We measured the DM from DART observation by calculating the time delay  $\delta t$  between time series

at two frequencies, 190 MHz and 205 MHz. The time series spans nearly 5 hours and includes 7 pulses, allowing us to establish a strong correlation between the two series. Nevertheless, the coarse time resolution (500 ms) and large pulse width prevent us from accurately measuring the delay.  $\Delta t$  is determined by fitting the cross-correlation relations between pulse series at two frequencies. For each correlation coefficient, it was derived by shifting the low-frequency series forward step by step.

Using the dispersion relation  $\Delta t = 4.148808 \times 10^3 \cdot (1/f_{190 \text{ MHz}}^2 - 1/f_{205 \text{ MHz}}^2) \times \text{DM}$ , one can derive the DM value through the  $\Delta t$ , at which the two series are most correlated. Our estimation shows that the time delay between 205 MHz and 190 MHz could be as long as ten seconds, and the corresponding DM is  $480 \pm 45 \text{ pc cm}^{-3}$ . The left panel of Fig.S5 shows the correlation coefficients versus the delay time (or DM) and our fitting results.

We measured the DM from FAST spectral by fitting the SNR of de-dispersed pulse at different DMs. The right panel of Fig.S5 shows the SNR of pulse de-dispersed under different DMs.

We measure the RM based on the spectrum observed by FAST. By using the `rmfit` tool of PSRCHIVE (42, 43), we got the RM estimation of  $+105.6 \pm 0.07 \text{ rad m}^{-2}$ .

## Emission Mode Changes

DART J1832-0911 exhibits several emission modes: wide-pulse, narrow-pulse, nulling (or weak emission below the detectability of DART), and dwarf pulse modes.

In the wide-pulse mode, pulses are typically strong, with widths around 200–250 s, whereas in the narrow-pulse mode, the pulses are much weaker, with widths of roughly 40–100 s. For most cases, the pulses remain consistent in both profile and strength, as shown in Fig.S1. However, we observed a significant disruption of this stability by dramatic changes on MJD 60439, where flux and profiles dramatically changed, as shown in Fig.S6. This sequence captures a transition from narrow-pulse to wide-pulse mode and back, with two strong wide pulses occurring within the narrow-pulse duration. Predictably, clear circular polarization components appeared at a fixed phase of the corresponding wide-mode pulse. The temporal evolution of the emission—from strong, wide pulses to weak, narrow ones, and eventually to quiescence—suggests a dynamic process of particle

accumulation and outward flow within the magnetosphere.

The dwarf pulse of DART J1832-0911 (illustrated in Fig.3) appears to be similar to those observed in some pulsars during their nulling states (*13, 14*). These sporadic, brief bursts are thought to arise from raindrops of particles formed via pair production close to the neutron star surface. That is, a gap model is the underlying mechanism responsible for the radio emission characteristics of LPT DART J1832-0911.

## **Polarization Characteristics**

During the emission-active epoch observed from DART, we found poor polarization in most pulses. Our recordings show three distinct polarization states. 1, Absence of Polarization: Both linear and circular polarization were largely undetectable throughout most of the emission cycle. 2, Transient Linear Polarization: A linearly polarized signal occasionally appeared as a short burst. Fig.S4 shows two instances of these bursts, where linear polarization coincided with an intensity spike in the total signal. Fig.S4 shows two instances of these bursts, where linear polarization coincided with an intensity spike in the total signal. 3, Phase-Locked Circular Polarization (CP): A stable, circularly polarized component appeared exclusively in the wide-pulse emission mode. Bottom panel of Fig.1 displays the phase-locked CP components recorded. Shaded areas in Fig.S4 and Fig.S6 highlight the CP profile ranges. These pulses include cases with reversed CP signs, cases with no sign change, and cases with no CP emission.

During the emission-quiet epoch observed with DART, we detected a bright burst due to the high sensitivity of FAST, with an estimated strength of 94 mJy , which is below DART's detection threshold. As shown in Fig.3, this pulse was highly linearly polarized, with linear and circular polarization degrees of 94% and 3%, respectively, and a flat position angle (PA) across the burst duration.

Our analysis supports an intrinsic properties of the phase-locked CP, suggesting that an intrinsic spin-down period rather than any extrinsic modulation consequence, e.g. an eclipse influence in a binary system and polarization conversion caused by SNR. During our observation period, both CP-active and CP-quiet states persisted for several days, as did the wide- and narrow-pulse

modes. Known binary systems are unlikely to remain in eclipse for multiple days. Furthermore, as shown in Fig.S6, CP appeared with burst signals even during the prolonged polarization-quiet period, implying no strict periodicity in the CP-active phases. The phase-locked CP may come from an open-field line region within magnetosphere of a pulsar. The sign change of CP is attributed to the magnetosphere emissions since the line of sight sweeps across the minimum angle between the line of sight and the magnetic axis. However, such non-LP property but with significant CP is rare for normal radio pulsars.

The high LP burst emitted during the DART’s non-detection period demonstrates a strong magnetic field of DART J1832-0911, such near 100% LP emission usually happens in some extreme emission phenomenons, like fast radio bursts (FRBs) ( e.g. (44–46)), and some of the giant pulse from radio pulsars (47, 48). Extremely high linear polarization places severe constraints on the radiation mechanism, only strongly magnetized sources can support relativistic particle bunches that emit highly linearly polarized signals. In addition, a flat PA, similar to some FRBs (44), indicates an intrinsic limited duration of the emitting process rather than a geometric affection. An emission scenario that plasma with insufficient density produces nearly 100% linearly polarized emissions and frozen PA from the strongly magnetized star surface to the exit point (where the wave undergoes poor rotation), with a short-lived timescale (49)

## Model Constraints

In addition to the direct observed proofs mentioned above, we discuss derived constraints about the nature of DART J1832-0911 in this section. According to the radio luminosity and emission duration, all reported LPTs are driven by coherent emission, same as transients like radio pulsars and FRBs, as shown in Fig.S2. However, emission from WD binary system ILT J11101+5521 is predicted also a coherent emitter (10). Therefore more constraints should be discussed.

**Neutron Star** We have demonstrated that DART J1832-0911 is likely a young neutron star that has been spun down due to interaction with an SNR fallback disk. Here, we further discuss this source under the assumption that it may be a spin-down powered neutron star. In an spin-down powered scenario, the magnetic field strength can be estimated using  $B \sim 6.4 \times 10^{19} \text{ G} \sqrt{P\dot{P}}$ , and

the spin-down luminosity is  $\dot{E} = 4\pi^2 I \dot{P} P^{-3}$  erg s<sup>-1</sup> where  $I = 10^{45} I_{45}$  g cm<sup>2</sup> is the moment of inertia (50–52). Taking into account the estimated age of DART J1832-0911, which is constrained by the evolution timescale of the associated SNR to be between  $3 \times 10^4$  and  $2 \times 10^5$  years, we can place limits on the magnetic field strength and spin-down luminosity. Specifically, the magnetic field strength limit is  $B' > 4 \times 10^{16}$  G and the loss rate of rotational energy is  $\dot{E} > 4 \times 10^{26}$  erg s<sup>-1</sup>.

We can compare the theoretically spin-down power to the emission power from the relation  $L_{\text{radio}} \approx 1 \times 10^{19} \left(\frac{\sin^2(\rho/2)}{\epsilon}\right) \left(\frac{D}{\text{pc}}\right)^2 \left(\frac{F}{\text{Jy}}\right) \left(\frac{f}{\text{MHz}}\right)$  erg/s, where  $\rho$  is the angular radius of the emitting cone and  $\epsilon$  is the pulse duty cycle (53). We assume a peak flux of the emission at  $F = 1$  Jy and the distance at  $D = 4.5$  kpc, taking a typical value (53) of  $\left(\frac{\sin^2(\rho/2)}{\epsilon}\right) \approx 10^{-2}$ , then the radio luminosity then can be estimated as  $L_{\text{radio}} \approx 8 \times 10^{26}$  erg/s.

We also discuss a spin-down mechanism caused by a supernova fallback disk. The braking process of a neutron star spun down by its surrounding supernova fallback disc is influenced by numerous aspects, including the initial mass  $M_{\text{d0}}$  and outer radius  $R_0$  of the disc, the neutron star's initial spin period  $P_0$  and magnetic field strength  $B_0$ , with the instability of the fallback disc playing a critical role as well. The evolution of spin angular velocity  $\Omega$  of the neutron star embedded in a fallback disk could be expressed as (34, 54):

$$I\dot{\Omega} = N_{\text{acc}} \cos \alpha + N_{\text{md}} + N_{\text{dip}}(1 + \sin^2 \chi) - \dot{I}\Omega, \quad (\text{S3})$$

where  $I$  is the moment of inertia of the NS,  $\alpha$  and  $\chi$  are the angle between the spin axis of the NS and rotation axis of the disk, and the magnetic inclination angle of the NS, respectively. The spin evolution of neutron stars assisted by fallback disks is mainly dominated by three torques: the accretion torque  $N_{\text{acc}}$ , the torques caused by magnetic field-disk interaction  $N_{\text{md}}$  and by magnetic dipole radiation  $N_{\text{dip}}$ . Among these,  $N_{\text{md}}$  plays a critical role in the formation of ultra-long-period pulsars.

Moreover, it should be noted that radio emission can only be detected when neutron stars are in the radio ejector phase, which occurs when the inner radius of the disk exceeds the light cylinder radius or the disk becomes passive. Similar to accretion disks in dwarf novae and transient X-ray binaries, the fallback disks would be subject to the thermal ionization instability once the outermost regions of the disk cool sufficiently (32). Under these conditions, the transport of material along the disk becomes inefficient, resulting in a passive disk and the cessation of its activity. The

minimum temperature required for a disk to remain active is approximately 300 K (55). Here we evolved one million systems, assuming that the initial distributions of  $M_{d0}$ ,  $R_0$ ,  $B_0$  and  $P_0$  follow as:  $\log(M_{d0}/M_\odot) \in [-7, -1]$ ,  $\log(R_0/R_s) \in [1, 6]$ ,  $\log B_0(\text{G}) \in [13, 16]$ , and  $\log P_0(\text{s}) \in [-3, 1]$ . The simulated results of  $P$  and  $\dot{P}$  at  $3 \times 10^4$  yr and  $2 \times 10^5$  yr, corresponding to the age estimate of SNR G22.7-0.2, are shown as green and purple shaded areas in Fig.2. It is clear that these LPTs can be well covered by the simulated distributions of ejectors, which may support the hypothesis that such LPTs may originate from interactions between young neutron stars and fallback discs.

**Magnetic White Dwarf ?** The radio-limited brightness temperature  $T_B$  provides constraints on the source quantities by examining the relationship between brightness temperatures and the size of the emitting region, which is derived from the Rayleigh-Jeans relation of the blackbody spectrum. The form is

$$T_B = \frac{c^2}{2\pi k} \left(\frac{D}{vR}\right)^2 F_\nu \approx 2 \times 10^{19} v_{\text{MHz}}^{-2} F_{\nu, \text{mJy}} D_{\text{kpc}}^2 \cdot \left(\frac{R}{R_\odot}\right)^{-2}, \quad (\text{S4})$$

here we use stellar radius  $R$  to refer to the region size. For the transient space At an observation frequency of  $\nu_{\text{MHz}} = 300$  MHz and a distance range of  $4 < D_{\text{kpc}} < 5$  kpc, we have deduced the estimation of the brightness against stellar radius as depicted in Fig.S7.

The  $T_B - R$  estimation favors a white dwarf with  $T_B \sim 10^{19}$  at radio wavelength. For reported radio WDs (or their binary systems), the estimated  $T_B$  is below  $10^{12}$  K (8). Consequently, the radio  $T_B$  of DART J1832-0911 is too much higher for a WD model.

Additionally, our optical observation also put constraints to the WD evolution timescale by relating its limited bolometric magnitude to the cooling progress. Before the crystallization, the cooling timescale  $\tau_{\text{cool}}$  of a hot WD is dominated by losing its thermal energy through black body radiation. Theoretically, the cooling time  $\tau_{\text{cool}}$  is a function of the WD luminosity  $L$ , WD mass  $M_{\text{WD}}$ , core atomic weight  $A$ . The approximation relation can be expressed as (56, 57)

$$\tau_{\text{cool}} \approx \frac{10^8}{A} \left(\frac{M/M_\odot}{L/L_\odot}\right)^{5/7} \quad \text{years} \quad (\text{S5})$$

where  $M_\odot$  and  $L_\odot$  are the solar mass and luminosity. The WD luminosity is  $L = 4\pi R_{\text{WD}}^2 \cdot \sigma T_{\text{eff}}^4$ . Assuming a typical WD with pure carbon core, then  $A = 12$ , the mass and radius are  $M = 0.6 M_\odot$  (58) and  $R_{\text{WD}} = 7,000$  km (59), respectively. We then obtained a cooling time  $\tau_{\text{cool}}$  should be longer than  $10^8$  years.

As WDs could be also spin-powered dominated (8), we can estimate the period derivation

**Table S1: The separations between the two nearby sources and the central coordinate of the DART location, as well as their  $r$ -band magnitudes.**

Source	Separation (arcsec)	Magnitude (mag)
s1	5.0	23.7
s2	7.2	23.1

according to the  $\tau_{\text{cool}}$  by the spin-down mechanism which can be expressed as  $\dot{P} = \frac{P}{2\tau_{\text{cool}}}$ . We assume that a radio WD is also a spin-down powered emitter, then the rotational energy loss rate could be the same type as the above neutron star case, but bias at the moment of inertia, which is  $I' \approx 10^{50}$  g cm<sup>2</sup> for a typical WD. Then we obtain the spin-down luminosity of a WD at  $\dot{E}' \sim 8 \times 10^{28}$  erg/s, which is much higher than the practical emission power. It shows that a spin-down powered WD cannot be responsible for LPT like DART J1832-0911.

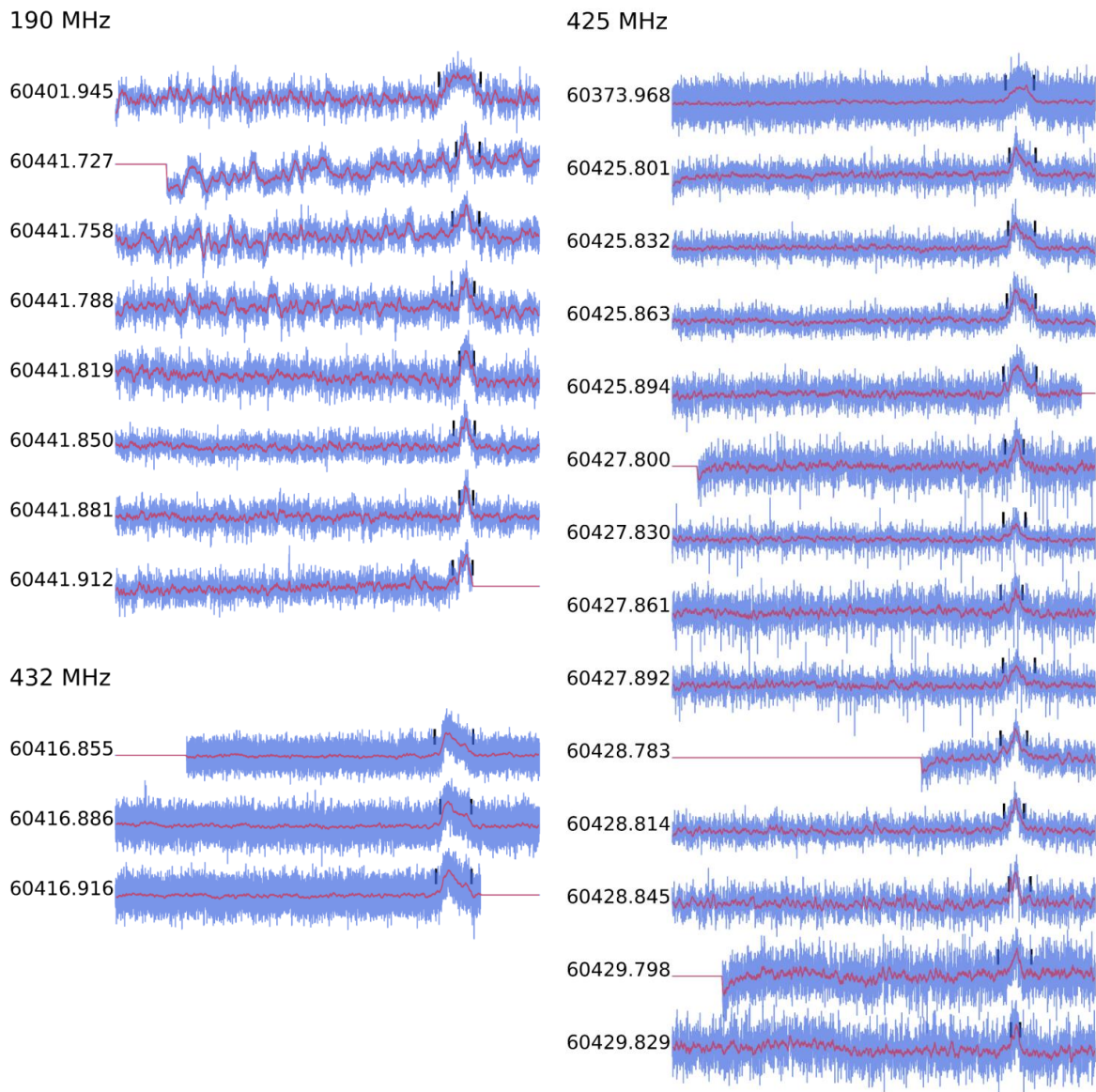


**Figure S1: Part of single pulse profile collected by DART.** We present a portion of the single pulse at 190 MHz, 425 MHz, and 432 MHz. The blue profiles are original samplings with different temporal resolutions, which are 100 ms (MJD 60373.968), 800 ms (MJD 60401.945), and 500 ms (others). The red profiles are smoothed series by running mean process.

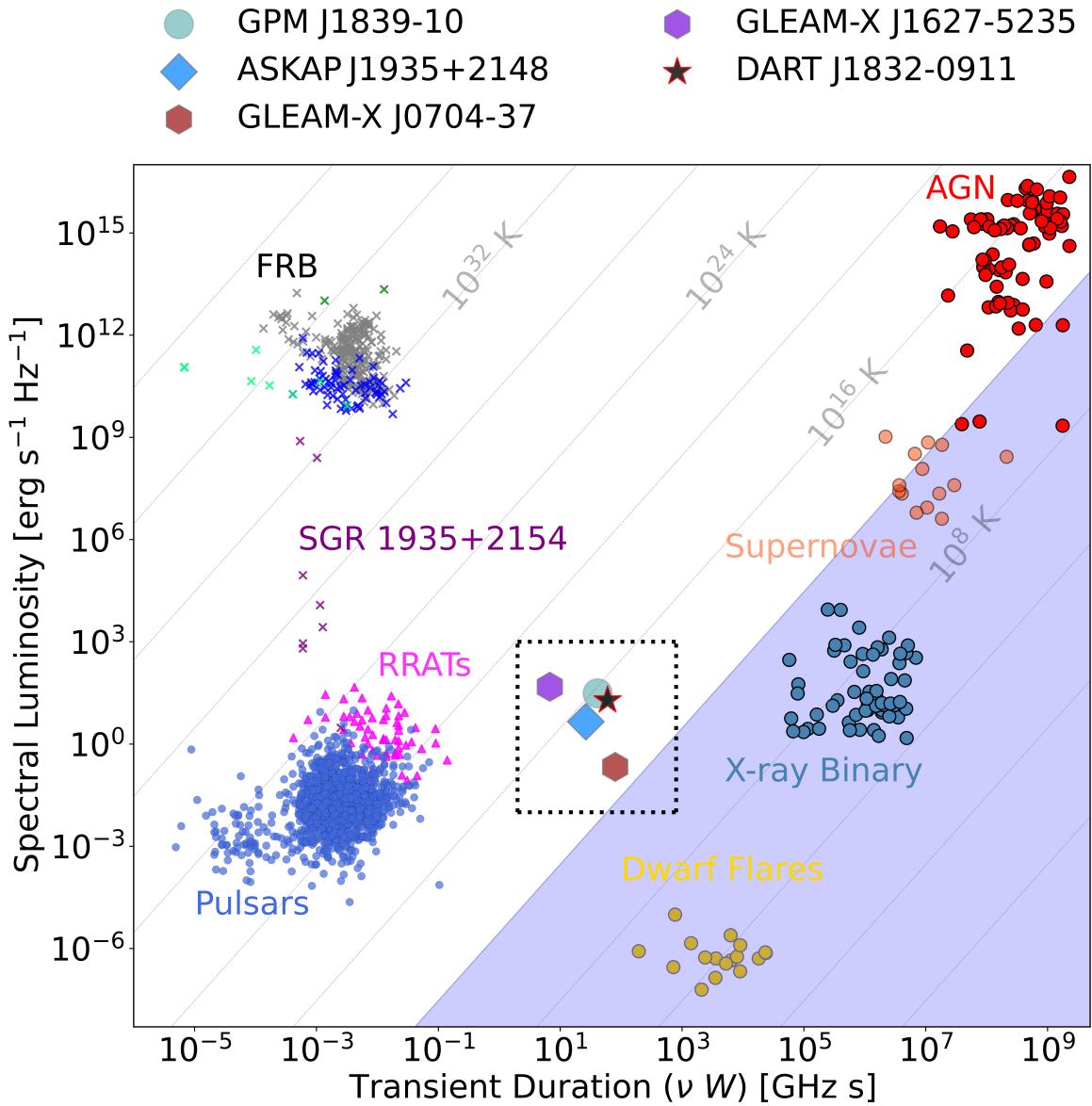


**Figure S2: Transient phase space diagram as a function of spectral luminosity against emission duration and frequency.** The LPTs cluster is marked in the black dashed box, of which the flux density and pulse width for the scatters of each LPTs are from the mean values provided from (1–3, 12). Grey diagonal lines indicate a limited brightness temperatures, which use  $cw$  to represent the region size in Equation.S4.

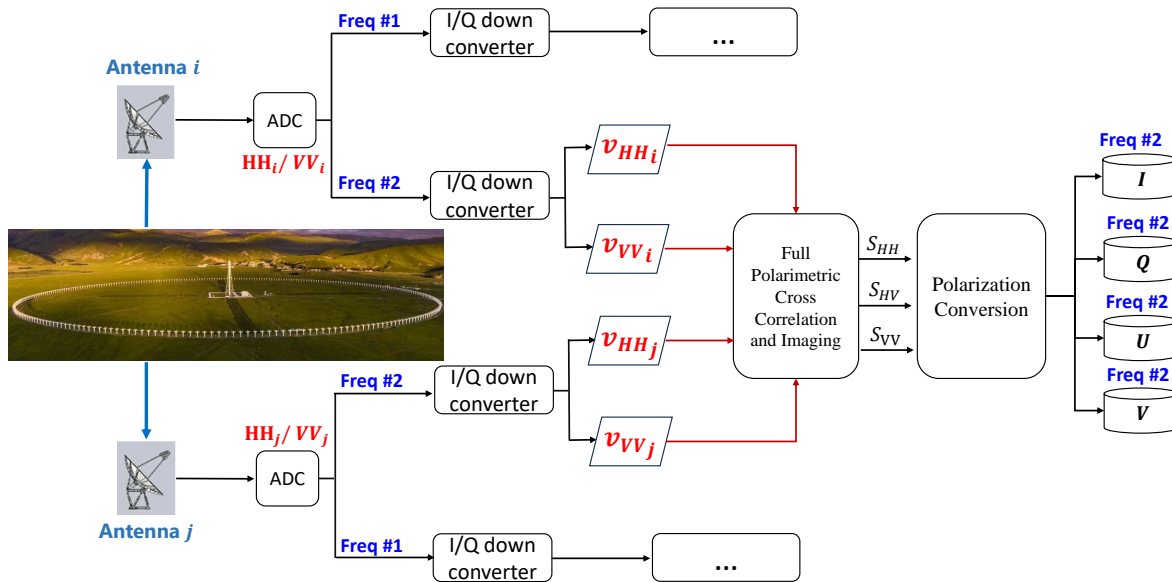


**Figure S3: Data processing pipeline of DART.** The raw data was recorded with full polarization at dual frequency. All samples of the continuous visibility function  $v_{HH}/v_{VV}$  from 626 links (comprising 313 antennas with two orthogonal polarizations) will undergo independent cross-correlation and imaging processing at each of the two frequencies.

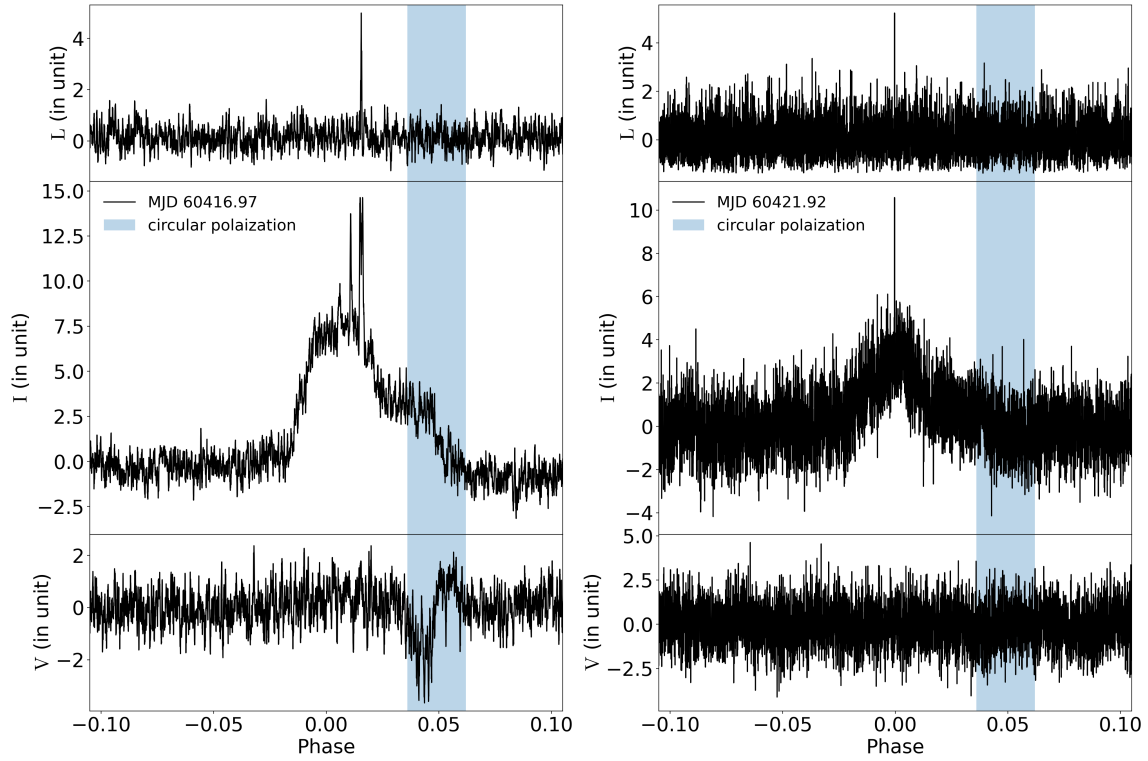


**Figure S4: The impulsive linear polarized burst (top panel) in two single pulses.** The temporal duration per bin for two pulses are 0.5 s for the left and 0.1 s for the right. Time series from the top to the bottom of each pulse are profile of LP, total intensity and CP.

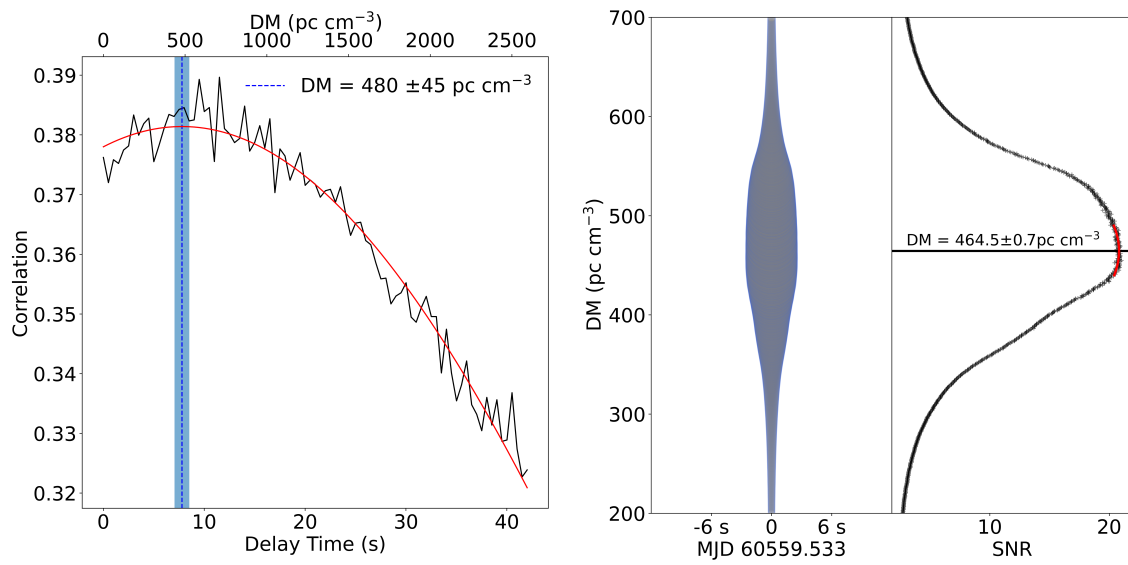


**Figure S5: DM estimation based on data from DART (left) and FAST (right).** DART: The function of correlation coefficient (black line) against delay time (i.e. DM) between time series at two frequencies. The red line depicts the fitting relation, and the blue range covers a confidence interval within  $1 \sigma$ . FAST: The single pulse search results.

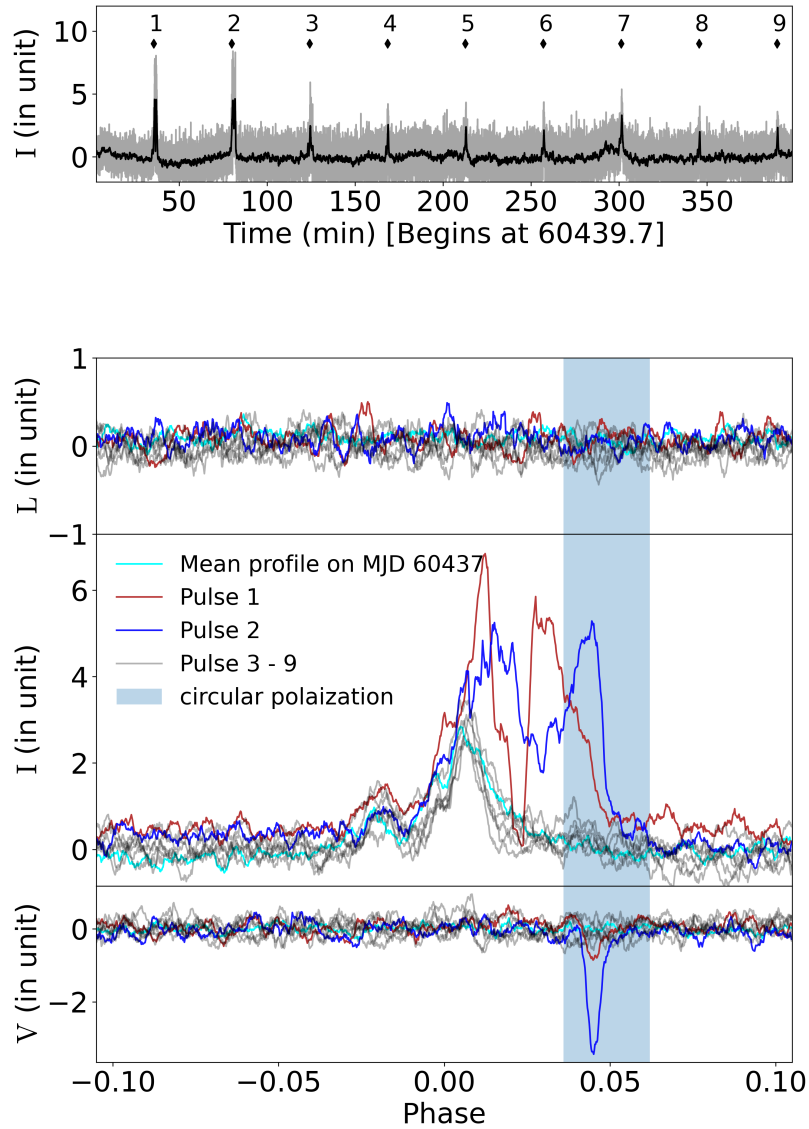


**Figure S6: A mode switching of DART J1832-0911 observed on 60439.7 (pulse 1-9).** The top panel is the time series of 9 continuous pulses. The three bottom panels are single pulse profiles of linear polarization ( $L$ ), total intensity ( $I$ ) and circular polarization ( $V$ ).

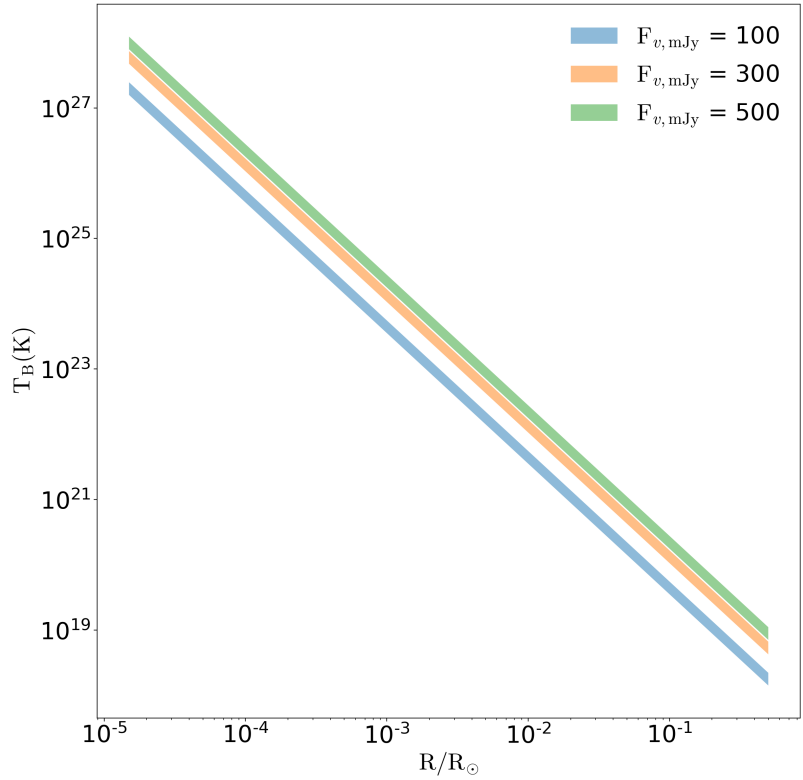


**Figure S7: The estimation of the radio brightness temperature against emitter radius.** The boundaries of each line correspond to the distance range from 4 to 5 kpc. The flux  $F_{\nu, \text{mJy}}$  are estimated mean intensities.

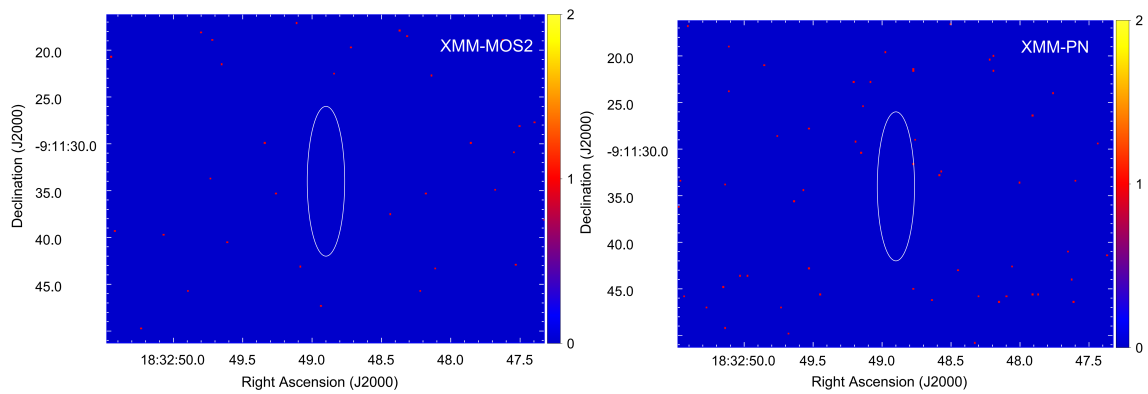


**Figure S8: The XMM-Newton image of DART J1832-0911.** The left and right panels represent the XMM-MOS2 and XMM-PN coverage of this source and the corresponding X-ray (0.2-10 keV) sky maps within positional error, respectively. The colorbars indicate the photon counts.